Results in Engineering 26 (2025) 104818

Contents lists available at ScienceDirect

Results in Engineering

journal homepage: www.sciencedirect.com/journal/results-in-engineering

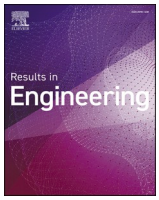

Research paper

Effect of duplex and austenite stainless steel fillers on mechanical, microstructural, and corrosion characteristics of dissimilar welds using Cold Metal Transfer welding

Saravanakumar Sengottaiyan [a], V.S. Shaisundaram [b], M. Shameer Basha [c], B. Deepanraj [d], N. Senthilkumar [e,*]

[a] Faculty of Engineering and Technology, Villa College, Male, 20002, Maldives
[b] Department of Automobile Engineering, Vels Institute of Science, Technology and Advanced Studies, Chennai, Tamil Nadu, 600117, India
[c] Department of Mechanical Engineering, College of Engineering, Qassim University, Buraydah, 51452, Saudi Arabia
[d] Department of Mechanical Engineering, College of Engineering, Prince Mohammad Bin Fahd University, Al Khobar, 31952, Saudi Arabia
[e] Saveetha School of Engineering, Saveetha Institute of Medical and Technical Sciences, Saveetha University, Chennai, Tamil Nadu, 602105, India

ARTICLE INFO

Keywords:
Cold Metal Transfer
Dissimilar joints
E2209 Filler
ER309L Filler
Microstructural analysis
Corrosion resistance

ABSTRACT

This research analyzes the mechanical, metallography, and corrosion characteristics of dissimilar (SS316L and SS439 stainless steels) weld joints developed with Cold Metal Transfer (CMT) technique with E309L and E2209 filler wires. SEM analysis of the WZs (WZ) showed that E309L exhibited a homogeneous structure with larger and more frequent pits in corrosion testing. In comparison, E2209 welds demonstrated finer dendritic structures with fewer corrosion pits, indicating superior resistance to pitting corrosion. Mechanical testing highlighted that E2209 welds achieved an improved ultimate tensile strength (582 MPa) and 74 MPa impact strength compared to E309L welds (525 MPa UTS and 62 MPa impact strength). However, E309L welds exhibited slightly better elongation (35 %) due to their fully austenitic structure. Microhardness analysis revealed that E2209 welds had higher hardness in the WZ (approximately 350 HV), attributed to their duplex microstructure. In contrast, E309L welds showed uniform but lower hardness values (~330 HV), and the potentiodynamic polarization tests were done in NaCl solution (3.5 wt. %) showed better corrosion resilience for E2209 welds, with has a reduced corrosion current density and a more favourable corrosion potential compared to E309L welds. SEM analysis of the corrosion morphology confirmed fewer and smaller pits in E2209 welds.

1. Introduction

Dissimilar metal joints find extensive usage in many engineering fields because they combine distinct mechanical, physical, and chemical properties to meet complex performance demands [1–3]. Joining dissimilar metals enhances operational performance by improving weight-to-strength ratios, reducing fabrication costs, and enabling application-specific property modifications [4–6]. However, welding dissimilar materials presents difficulties caused by variations in chemical composition, melting points, and thermal expansion, often leading to defects such as brittle fractures and intermetallic phase formation [7–9]. The Cold Metal Transfer (CMT) welding technique is an effective solution for welding dissimilar materials, offering controlled input of heat, nominal distortion, and minimized residual stress [10,11]. This method ensures stable arc conditions, improved metal transfer, and enhanced weld quality. Achieving reliable dissimilar joints through CMT welding relies heavily on two critical factors: filler material selection and microstructure control [12,13]. In industrial applications, stainless steels SS316L and SS439 are frequently selected for their unique properties [14,15]. SS316L, an austenitic stainless steel, offers outstanding corrosion resilience, mechanical strength, and ductility, making it ideal for marine and chemical environments [16,17]. Conversely, SS439, ferritic stainless steel, is valued for its superior thermal conductivity, oxidation resistance, and cost-efficiency, making it suitable for high-temperature applications [18,19]. E309L and E2209 fillers are commonly employed to overcome the challenges encountered during welding. E309L, an austenitic filler, provides good weldability and ductility but may show increased pitting corrosion susceptibility in

* Corresponding author.
E-mail addresses: saiswastik23@gmail.com (V.S. Shaisundaram), nskmfg@gmail.com (N. Senthilkumar).

https://doi.org/10.1016/j.rineng.2025.104818
Received 2 February 2025; Received in revised form 20 March 2025; Accepted 5 April 2025
Available online 6 April 2025

Table 1
Base Materials Mechanical Features.

BM	UTS (MPa)	Elongation %	Yield Strength (MPa)	Hardness (HV)
SS316L	485	40	170	217
SS439	438	28	265	250

Table 2
Chemical Configuration of Metals and Fillers (wt. %).

Material (%)	C	Cr	Ni	Mn	Mo	Fe
SS316L	0.03	17.153	10.13	1.513	2.062	Balance
SS439	0.01	17.35	0.2	0.25	0.1	Balance
ER309L Filler	0.03	19	11.5	1.8	2.8	Balance
E2209 Filler	0.02	22.87	8.54	1.04	3.10	Balance

aggressive environments [20]. E2209, a duplex stainless-steel filler, combines ferrite and austenite phases, enhancing tensile strength, toughness, and corrosion resistance. This study investigates the impact of E309L and E2209 fillers on the mechanical, microstructural, and corrosion features of SS316L-SS439 dissimilar welds produced using CMT welding. The findings aim to guide filler material selection for improved weld performance in demanding applications.

Several studies have investigated the impact of different filler materials on the mechanical, microstructural, and corrosion characteristics of dissimilar stainless-steel welds. Varma et al. [21] examined the performance of E309L, E309LMo, and E2209 fillers in welding 2205 duplex stainless steel with SS316L, reporting that E2209 welds exhibited superior pitting corrosion resistance, higher strength, and improved hardness due to their duplex microstructure, while E309L provided better ductility and intergranular corrosion resistance. Shojaati and Beidokhti [22] found that ER2209 outperformed ER310, ER316L, and nickel-based fillers in strength and hardness, while ER316L improved ductility, but nickel-based fillers faced fusion line cracking issues. Tembhurkar et al. [23] demonstrated that ER316L welds offered higher tensile strength and toughness, whereas ER309L welds showed superior pitting corrosion resistance due to a higher Creq/Nieq ratio. Wang et al. [24] highlighted that martensitic phase formation reduced corrosion resistance in AISI 304/AISI 430 welds with increased nickel content, but adding chromium enhanced corrosion resistance. Gupta et al. [25] studied CMT welding of SS304L and SS439, revealing that low heat input promoted dense lathy ferrite formation, enhancing tensile strength and hardness, while higher input of heat enhanced the corrosion resilience. Ambade et al. [26] reported that ER309L welds exhibited better hardness and toughness than ER316L, while ER316L demonstrated improved tensile strength and elongation. Further, Verma et al. [27] found that E2209 welds, due to their duplex microstructure, provided superior resistance to corrosion and mechanical properties compared to E309LMo welds, which offered good film characteristics but lower pitting resistance. Collectively, these studies emphasize the influence of filler material selection, phase balance, and welding variables on achieving optimal mechanical and corrosion resistance features in stainless-steel dissimilar welds.

Previous studies have demonstrated that filler materials, welding techniques, and thermal input significantly influence the mechanical characteristics and corrosion resilience of different stainless steel weld joints. However, existing literature lacks a comparative investigation of E309L and E2209 fillers in welding SS316L and SS439 using the CMT process. Furthermore, limited research addresses the combined influence of welding variables on microstructural evolution, mechanical properties, and electrochemical behaviour in such joints. This study presents a novel investigation that addresses this gap by examining the performance of E309L and E2209 fillers in SS316L-SS439 weldments. While these fillers have been widely studied with other materials, no prior research has explored their combined effects in this specific

Table 3
CMT-Welding Parameters.

Filler Material	Welding Speed (mm/s)	Current (A)	Voltage (V)	Heat Input (kJ/mm)	Deposition Rate (kg/h)
E2209	3.2	120	25	2.1	0.741
ER309L	3.4	120	23	1.93	0.767

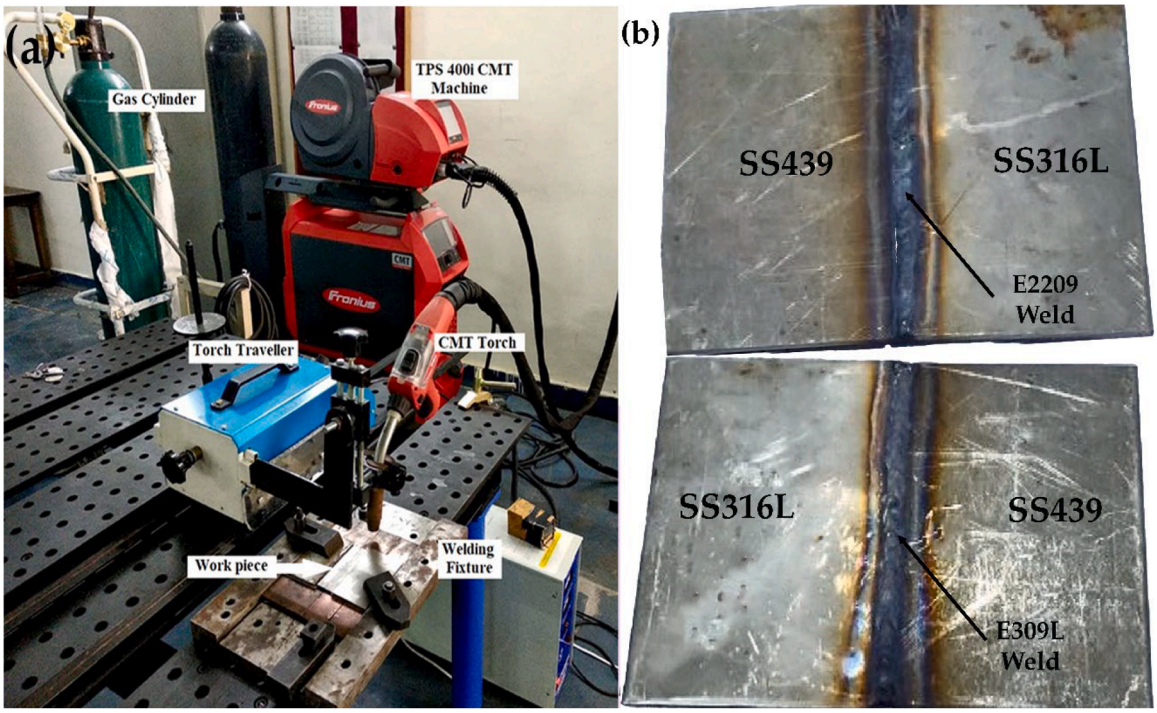

Fig. 1. Fabrication of dissimilar joints.

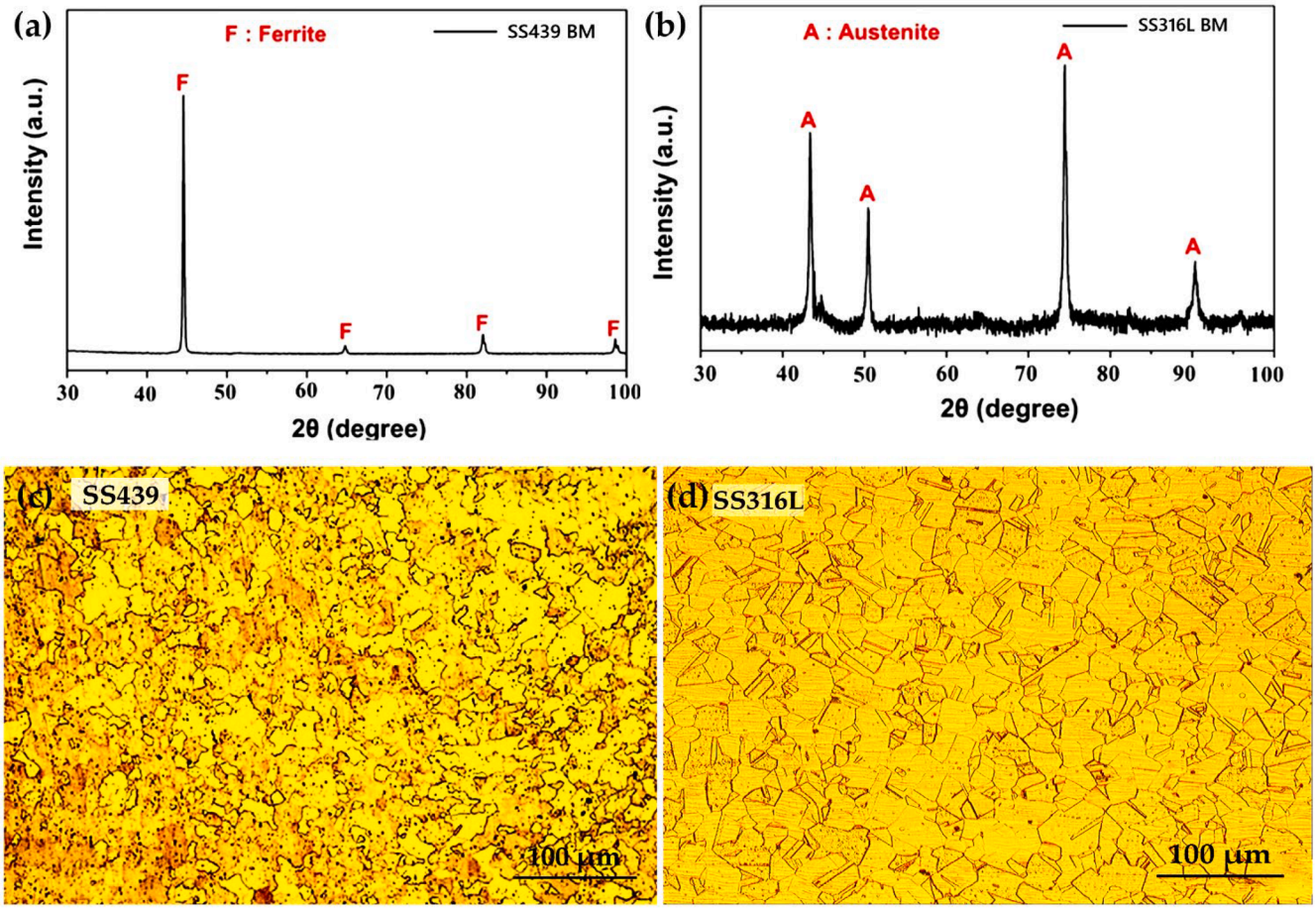

Fig. 2. XRD and Optical Microscopy analysis of BMs.

material combination. The study employs advanced characterization procedures viz., EBSD, XRD, and element mapping to analyze phase evolution, grain structure, and elemental distribution across the weldment. This study provides new insights into optimizing weld stability and durability by correlating microstructural changes with mechanical performance and corrosion resistance. The findings offer practical guidance for industries such as marine, petrochemical, and heat exchanger systems while contributing to sustainable engineering practices by promoting material longevity and reducing maintenance costs, aligning with SDG 9 and SDG 12.

2. Materials and methods

2.1. Materials

The two stainless steel grades, SS316L and SS439, were the primary basis for this research, industries have adopted SS316L as a standard material because its excellent mechanical strength, weldability capabilities, and strong corrosion resistance make it exceptionally effective [26]. The base materials properties are enumerated in Table 1.

SS439 finds its application within structural and automotive fields due to its outstanding heat conductivity alongside exceptional oxidation resistance. Before welding, both materials underwent heat treatment to relax internal stresses and establish microstructural stability. The main structural elements of the SS439 sample were subjected to an 800 °C temperature for sixty minutes during annealing, while SS316L required a 1000 °C temperature maintenance for sixty minutes. Both materials underwent water quenching immediately after reaching their target temperatures. The welding operation needed two kinds of filler materials, E2209 and E309L. E2209 consists of an austenitic-ferritic structure as part of its filler metal status, and its mechanical integrity and corrosion resistance capability receive reinforcement from high chromium (Cr) and molybdenum (Mo). The resistance to heat cracking and strength enables austenitic stainless-steel filler E309L to join metals that generally cannot be welded together [28]. This study used filler wires and base metals (BMs) whose chemical onion compositions are depicted in Table 2.

2.2. Fabrication

SS316L and SS439 were joined using the GMAW process in CMT mode. The TPS400i CMT machine (Fig. 1(a)), chosen for its ability to regulate heat input, exhibit little spatter, and weld dissimilar materials. The SS316L and SS439 plates, measuring 120 × 75 × 3 mm^3, were meticulously cleaned to eliminate oxides, oil, and contaminants from their surfaces. These preparations reduced the frequency of defects throughout the operation and achieved optimal weld quality [29]. Two filler wires with a diameter of 3.2 mm, E2209 and ER309L, were used in the welding process. E2209 enhances chloride resistance and improves mechanical qualities for duplex stainless-steel fillers. ER309L, an austenitic stainless-steel filler, is the most favoured choice for dissimilar welds because of its excellent weldability and thermal stability. A uniform butt joint configuration with a 1.2 mm root gap was consistently used throughout the welding procedure (Fig. 1(b)). To avert oxidation and the ingress of impurities into the weld pool, the shielding gas used was standard argon gas, flowing at a rate of 8 L/min. The selection of this shielding gas decreased spatter formation, improved weld quality, and facilitated a stable arc. The welding current, voltage, speed, and heat input to achieve the necessary weld quality were established, regulated, and customized to optimize the joints' resistant to corrosion,

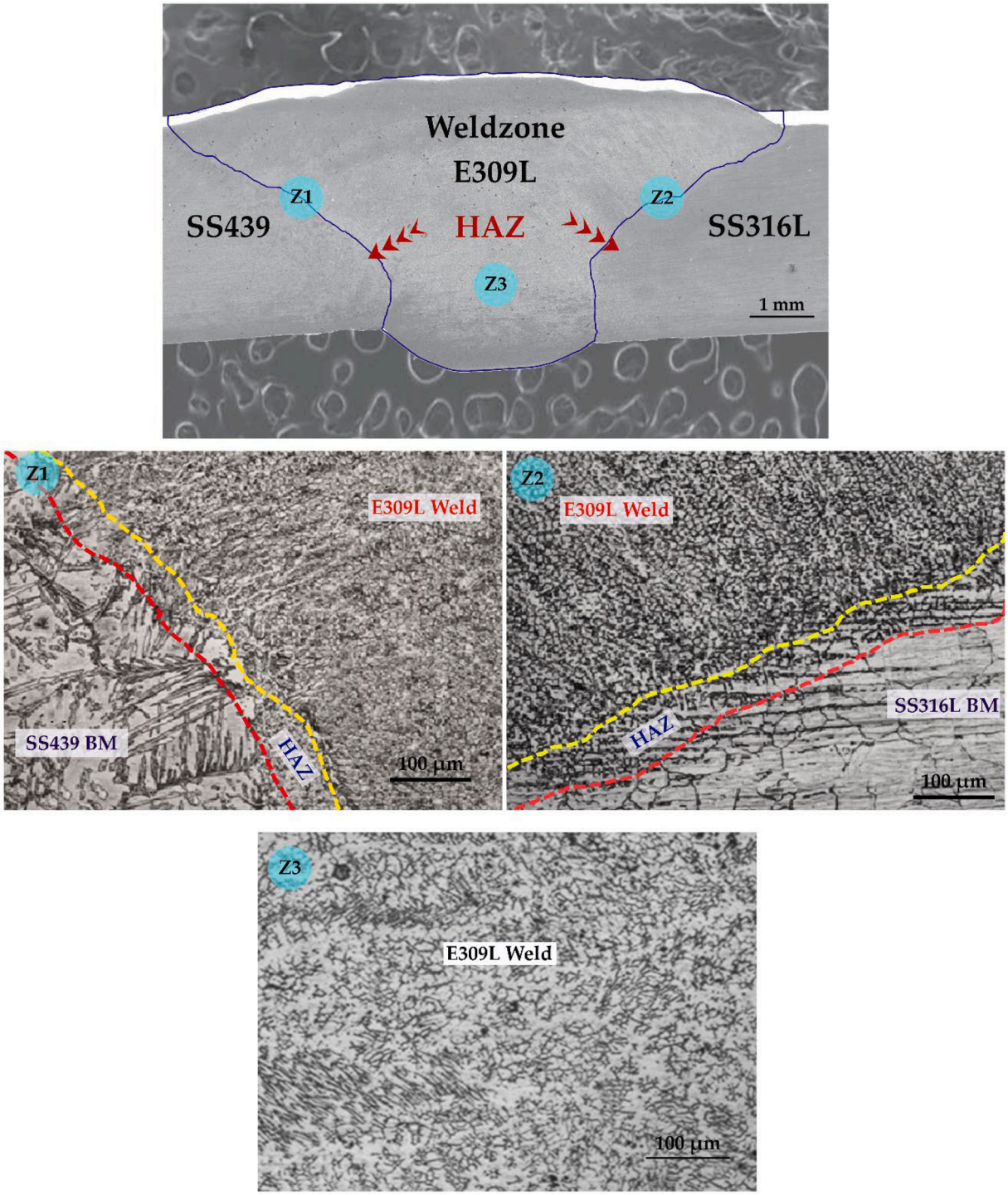

Fig. 3. Microstructure analysis of E309L weld.

microstructural integrity, and mechanical characteristics. The heat input (HI) and deposition rate (DR) were determined using Eqs. (1) and (2) [26].

$$HI = \frac{\eta \times V \times A}{w} \ (kJ/mm) \quad (1)$$

$$DR = A_w \times F \times \rho * 3600 \ (kg/h) \quad (2)$$

Where V represents the voltage (volts), A denotes the welding current (A), w signifies the welding speed (mm/s), and η indicates the efficiency of the GMAW-CMT process, assumed to be 0.7. DR is calculated based on the cross-section area of wire, wire feed rate and filler density. Heat input is a crucial determinant that affects the weld microstructure, mechanical characteristics, and distortion. A regulated and moderate heat input is essential to equilibrate penetration depth and reduce thermal damage to the BMs. Table 3 presents the specific welding settings for each filler material [30].

During welding testing, a speed of 3.2 mm/s and 3.4 mm/s is maintained for E2209 and ER309L. Adequate fusion of BMs and filler wire was preserved with lower welding current and voltage levels, preventing welding defects such as porosity and cracking. Because E2209 filler combines duplex stainless steel, it needs increased heat

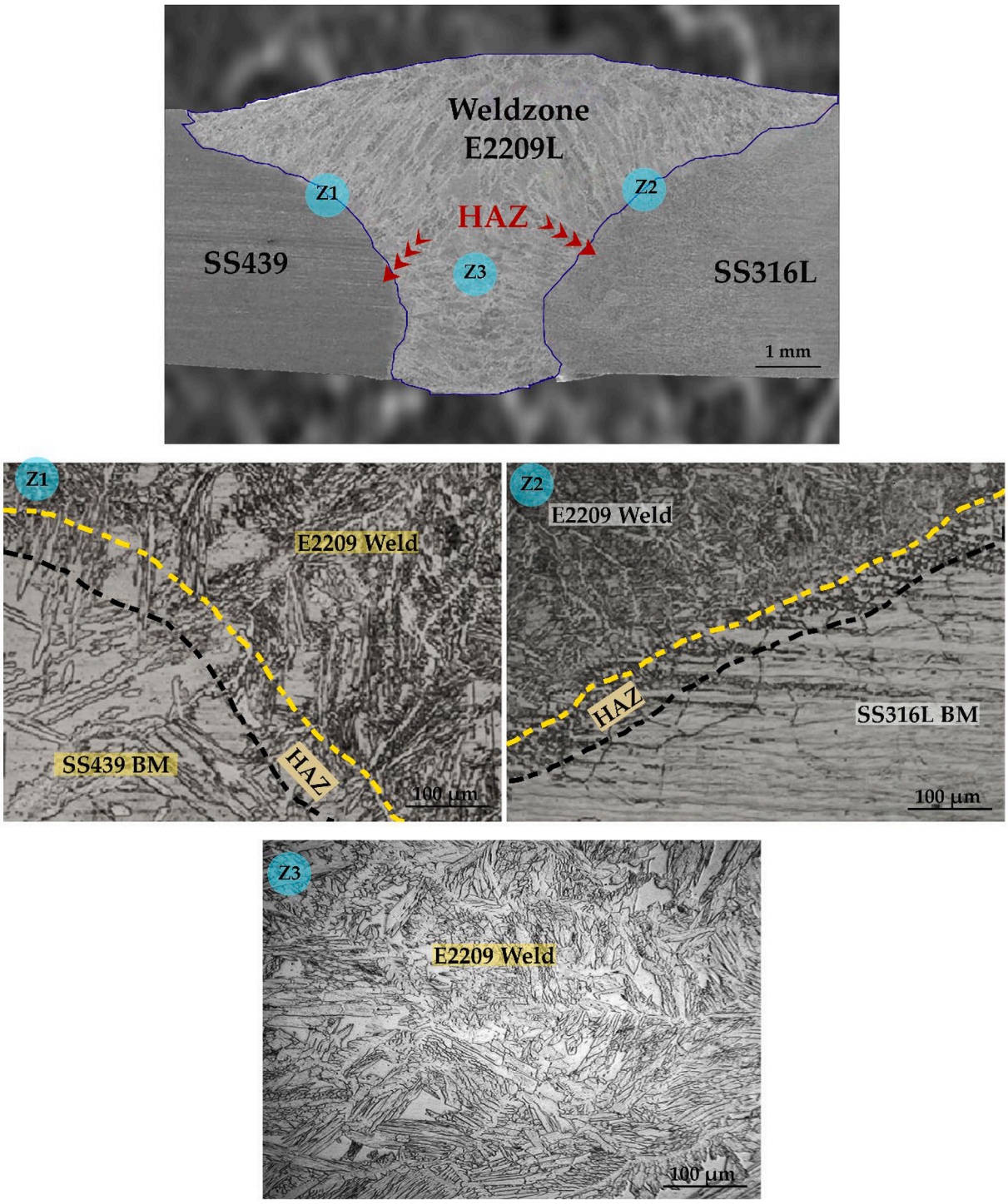

Fig. 4. Microstructure analysis of E2209 weld.

input yet delivers superior mechanical performance and corrosion resistance. Through precise arc control, GMAW-CMT welding managed to lower heat input levels, thereby protecting the heat-affected zone (HAZ) and resulting in smooth, defect-free weld beads. With the CMT technique, precise deposition rate control produced stable weld quality levels.

2.3. Microstructure analysis

Samples measuring 10 × 10 × 3 mm^3 were extracted from the joints for microstructural evaluation. Different SiC abrasive sheets of varying grits were used to polish the specimens successively before they received a final polish using a 0.75 µm alumina slurry on velvet fabric, followed by ultrasonic cleaning [31,32]. The BM and weldment were prepared for visualization of microstructure by performing electrochemical etching in an oxalic acid (10 wt. %) solution. Electrochemical etching was applied at a 1 A/cm^2 current density throughout the 90-second process duration. A Zeiss Axio Lab optical microscope analyzed selected weld positions in the HAZ and weld zone (WZ).

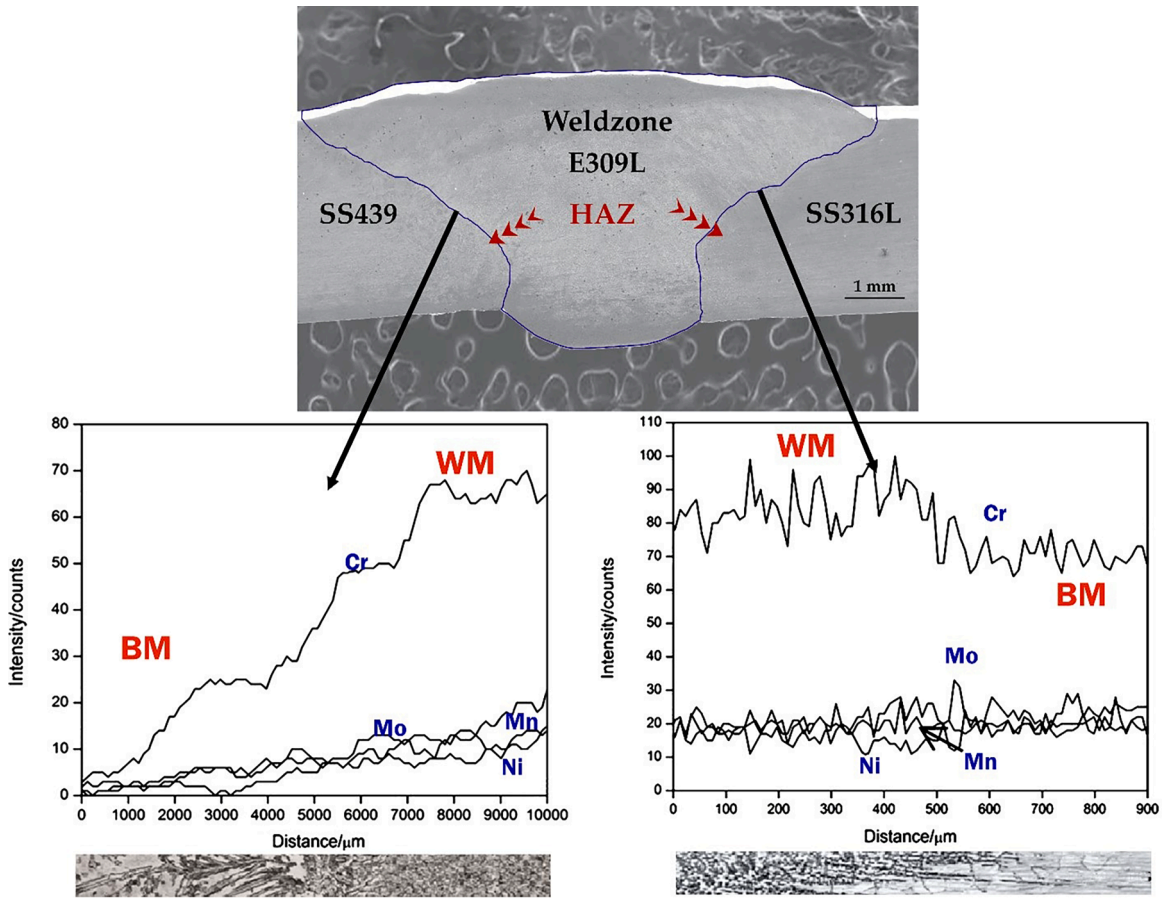

Fig. 5. Element Distribution of E309L Weld.

2.4. Mechanical properties

Investigations were done to test the performance strength of weldments, and the tensile testing procedure was executed on welded plate specimens following ASTM E8 standard methodology [25]. The mechanical capabilities of the welds were assessed by obtaining the UTS and elongation percentage (EL %) measurements [33]. Vickers microhardness tester analyzed the hardness of the WZ and adjacent HAZ with BM regions with 500 g force in the junction weld, adopting ASTM E384 [34]. In accordance with ASTM E23, the Charpy impact test was used to assess the toughness of the dissimilar weld joints. The impact specimens were extracted from the WZ with their notch positioned at the fusion zone to assess the weld interface's resistance to impact loading, aligned perpendicularly [35]. Each specimen had standard dimensions of 55 × 10 × 10 mm^3 with a 2 mm V-notch depth and a Ø0.5 mm notch tip.

2.5. Corrosion test

Potentiodynamic polarization studies investigated how E309L and E2209 weld samples reacted to corrosion when submerged in a NaCl solution (3.5 wt. %) at ambient conditions while operating through a three-electrode setup as per ASTM G5–14 [36]. Analysis used weld specimens as working electrodes after they were engraved in epoxy resin with exposed surface of 0.50 cm^2, together with platinum counter electrodes and saturated calomel reference electrodes. First, the specimen surfaces underwent polishing with 1200-grit materials before they received distilled water rinsing and hot air-drying treatment. Likewise, polarization testing unfolded through a 0.5 mV/s rate, which moved from the natural corrosion potential to +1200 mV compared to SCE [37]. The test was done thrice to verify repeatability, followed by an SEM analysis of the specimen's corrosion morphology.

3. Results and discussion

3.1. Microstructure analysis of BM

A microstructural examination conducted by employing X-ray diffraction (XRD) and optical microscopy techniques identifies their distinct structural phases and grain morphologies, which determine their welding capabilities and functional performance. XRD examination of SS439 shows (Fig. 2a) ferritic phase peaks demonstrating a body-centred cubic (BCC) structure. High-temperature applications greatly benefit from the oxidation-resistant and thermally stable properties of SS439′s ferritic structure [38]. The XRD pattern shown in Fig. 2b for SS316L contains noticeable peaks that signify an austenitic face-centred cubic (FCC) geometry structure. Austenitic phase characteristics determine SS316L's outstanding mechanical properties and corrosion resistance alongside ductility, which makes it highly suitable for industrial use. A uniform structure characterized by the absence of added phases in both materials finds suitability for dissimilar welding processes. SS439 exhibits polygonal ferrite grains with uneven borders, indicating superior thermal conductivity and resistance to grain development at high temperatures (Fig. 2c). Conversely, SS316L displays equiaxed grains with distinct boundaries, typical of annealed austenitic stainless steel, improving its mechanical strength and resistance to thermal stress (Fig. 2d) [39]. The greater grain size of SS439 relative to SS316L indicates variations in thermal expansion characteristics critical factors during welding [40].

3.2. Microstructure analysis of E309L & E2209 weld

The microstructural investigation (Fig. 3) of the E309L weld in the dissimilar joint between SS316L and SS439 reveals distinct transition

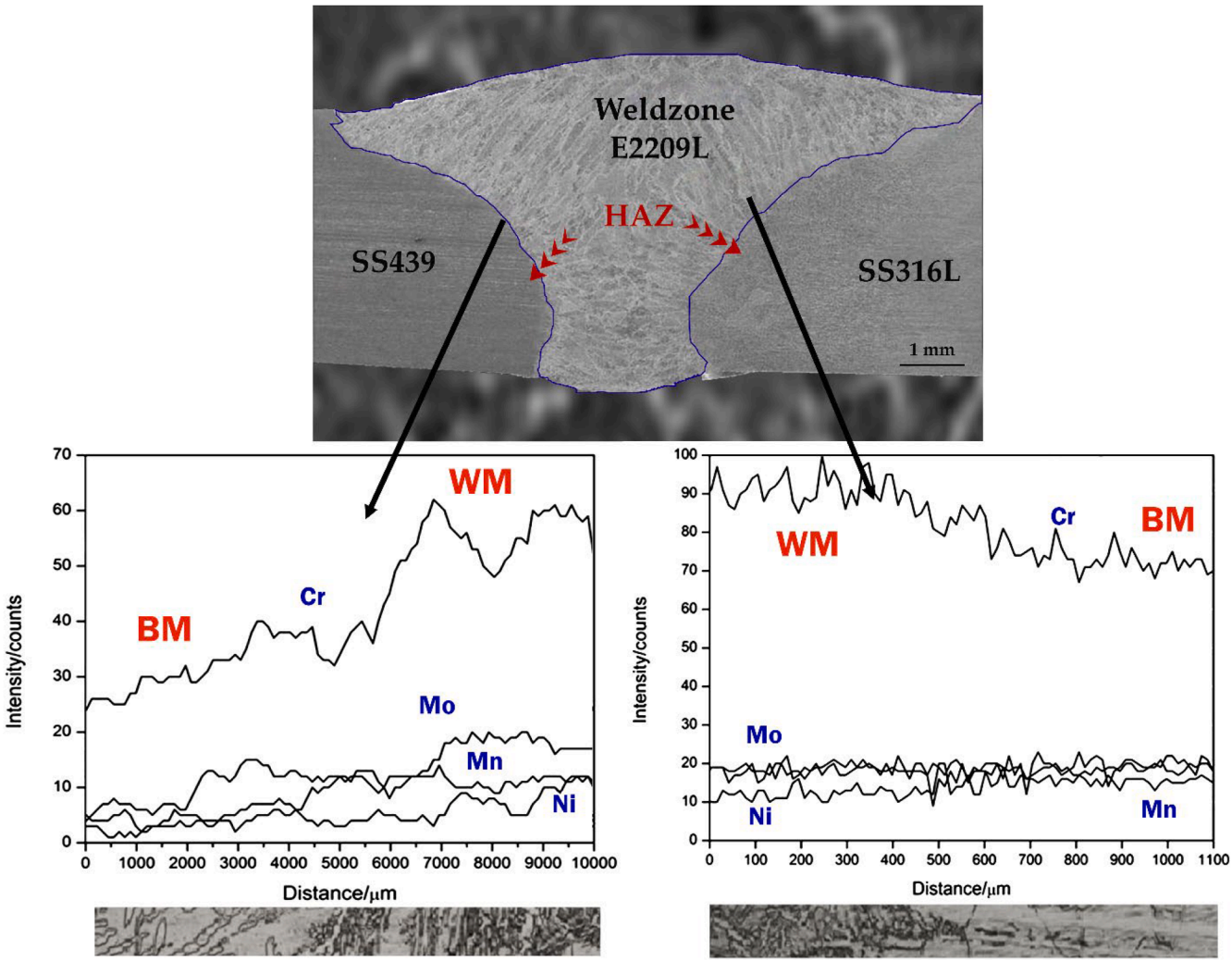

Fig. 6. Element distribution of E2209 weld.

zones and weld metal characteristics. The SS439 side (Z1) exhibits a HAZ characterized by coarse ferritic grains, signifying a evolution from the ferritic BM microstructure to the weld metal [41]. A distinct boundary is observed between the ferritic stainless steel and the weldment, clearly defining the transition zone. The HAZ displays a softer boundary on the SS316L side (Z2), preserving the BM's austenitic structure. The grains in this region remain finer due to the enhanced thermal stability of SS316L, which resists grain growth during welding. Structural integrity is maintained at this interface, where the E309L filler material effectively complements the austenitic matrix, minimizing the risk of brittle phases [42]. The weld metal (Z3) predominantly features an austenitic matrix structure interspersed with vermicular ferrite particles. This ferritic-austenitic solidification mode is characteristic of E309L filler material, enhancing ductility and thermal stability. While the E309L weld demonstrates excellent metallurgical bonding, micro-pores were identified during SEM analysis attributed to gas entrapment and rapid solidification during the CMTs process. Combining an austenitic matrix with dispersed ferrite in the WZ enhances ductility and mitigates the risk of hot cracking.

The microstructure of the E2209 weld (Fig. 4) at the SS316L-SS439 junction shows distinct metallurgical variations throughout the WZ (Z3) and both heat-affected regions (Z1 and Z2). The HAZ area within Zone Z1 of SS439 demonstrates a transition that converts from the BM ferritic microstructure into a duplex weld metal composition. The HAZ side develops coarse ferritic grains and lathy ferrite structures through material transformations because the welding temperature cycle creates grain growth while inducing partial phase changes. In the Z2, the heat-affected section shows steady microstructural changes because the E2209 filler works well with the base steel, maintaining the original austenitic structure. Superior heat stability in the austenitic stainless steel becomes apparent when the side of the HAZ shows finer granules compared to the SS439 side. Zone Z3 of the welded metal shows a duplex microstructure because of the balanced distribution between ferritic and austenitic phases. Grain boundary austenite alongside regular austenite presence strengthens mechanical performance and enhances the corrosion resistance of welds.

3.2.1. *Element distribution analysis of E309L and E2209 weld*

The element distribution maps (Fig. 5) illustrate the concentration variations of key alloying elements molybdenum (Mo), chromium (Cr), nickel (Ni), and manganese (Mn) across the BM, WZ, and HAZ in the E309L weldment joining SS439 and SS316L highlighting effective fusion. The Cr distribution shows a gradual increase from the SS439 BM to the weld, peaking in the WZ where the E309L filler composition is prominent, followed by a gradual decrease towards the SS316L side. This Cr gradient indicates diffusion across the weld interface, contributing to enhanced corrosion resistance in the weldment. Mn, Mo, and Ni distributions are more stable, with slight regional fluctuations. The nickel content is notably higher in the weld metal, aligning with the austenitic structure of the E309L filler, which stabilizes the weld's

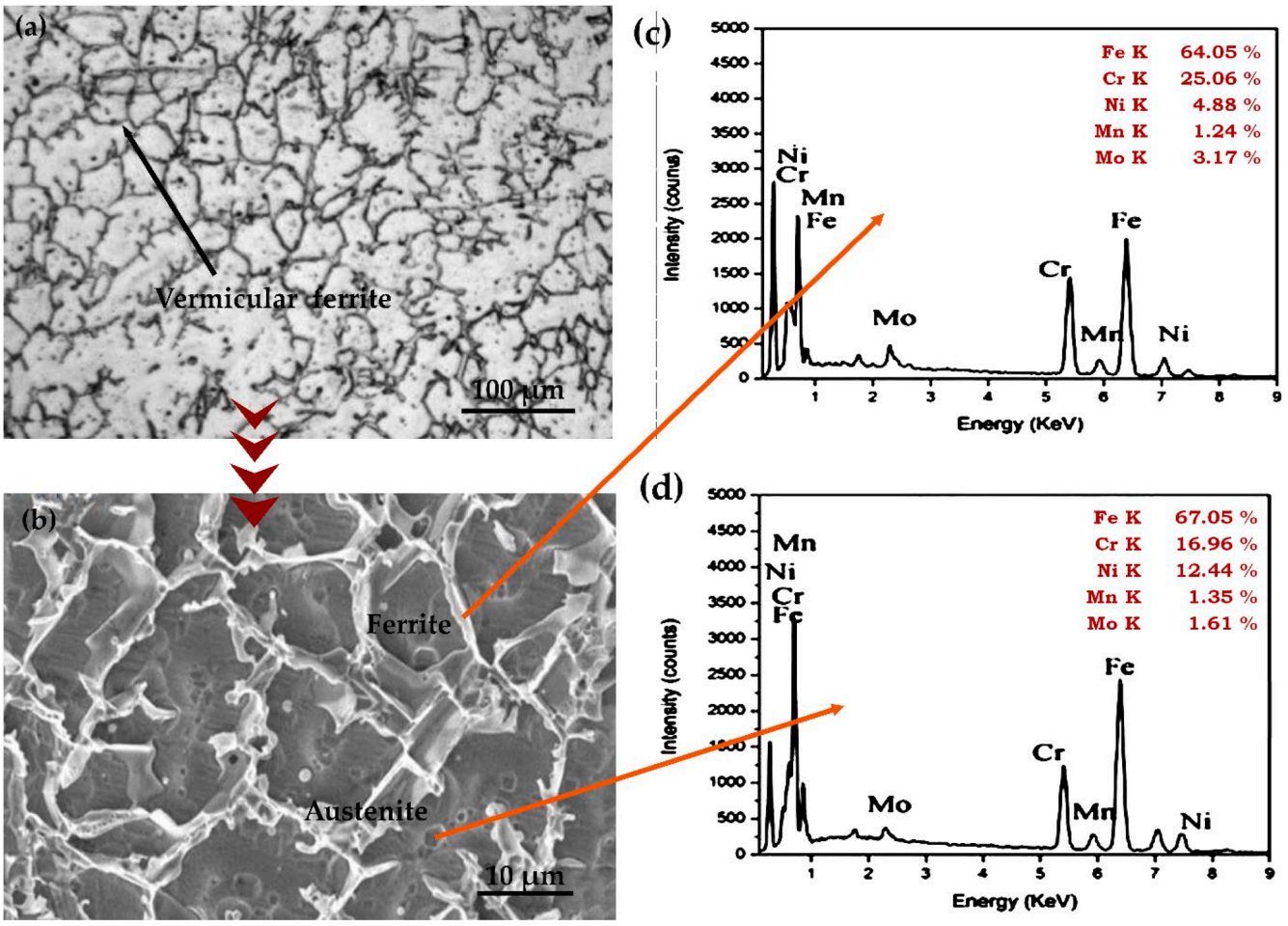

Fig. 7. SEM and EDS analysis of E309L weld.

microstructure. The presence of Mo in moderate amounts further enhances the weld's resistance to pitting corrosion.

The element distribution maps of the E2209L weldment are shown in Fig. 6. The Cr distribution shows a steady increase from the SS439 BM towards the weld metal, peaking within the WZ, followed by a gradual decrease towards the SS316L side. This Cr distribution indicates effective diffusion and improved corrosion resistance in the weldment. Mo shows stable concentrations with minimal fluctuations, ensuring enhanced pitting corrosion resistance. Ni content is notably higher in the weldment, stabilizing the austenitic phase in the duplex E2209L filler, contributing to improved toughness and mechanical strength. Manganese distribution remains relatively stable with no significant segregation, contributing to uniform microstructure formation.

The E2209L weldment offers superior corrosion resistance and mechanical stability compared to the E309L weldment due to better Cr and Mo distribution, improved Ni stabilization, and a more refined microstructure, making E2209L a preferable filler for demanding applications requiring enhanced durability and corrosion resistance.

3.3. SEM and EDS analysis of E309L weld

To examine the microscopic structure and the elements of the E309L WZ, SEM imaging and Energy Dispersive Spectroscopy (EDS) were used. Figs. 7(a) and 7(b) depict the microstructural structures of the E309L weld, while Figs. 5(c) and 5(d) present the corresponding EDS spectra confirming elemental composition. In Fig. 7(a), taken at 100 μm magnification, the microstructure exhibits a dual-phase configuration comprising vermicular ferrite and austenite. The vermicular ferrite phase appears as interconnected, web-like structures within the austenite matrix. The formation of such a structure is attributed to the substantial content of Ni and Cr in the E309L filler, which stabilizes both the ferrite and austenite phases during solidification. The presence of vermicular ferrite in the austenite matrix contributes to enhanced structural stability by mitigating hot cracking during welding [43]. Fig. 7(b), captured at higher magnification (10 μm), reveals the detailed distribution of ferrite and austenite phases. Ferrite forms an intricate network pattern, while austenite appears as well-defined grains interspersed within the structure [44]. This phase distribution is crucial for balancing the weld's mechanical strength and corrosion resistance.

The corresponding EDS spectra in Fig. 7(c) and (d) confirm the elemental composition of the identified phases. The ferrite phase (Fig. 5 (c)) contains 64.05 wt. % Fe, 25.06 wt. % Cr, and minor elements such as 4.88 wt. % Ni and 3.17 wt. % Mo, indicating a stable ferritic structure with improved resistance to pitting corrosion. Meanwhile, the austenite phase (Fig. 5(d)) shows a slightly higher nickel concentration (12.44 wt. % Ni) with 67.05 wt. % Fe and 16.96 wt. % Cr, which supports enhanced ductility and corrosion resistance. This SEM and EDS analysis confirms that the E309L weld exhibits a stable dual-phase microstructure, combining the structural benefits of ferrite with the corrosion resistance and ductility of austenite [45].

3.4. SEM and EDS analysis of E2209 weld

Fig. 8(a) reveals E2209 WZ phases under 100 μm lower magnification, unlike austenite alongside ferrite intermixed throughout the structure. Elongated austenite islands exist within the ferritic matrix to

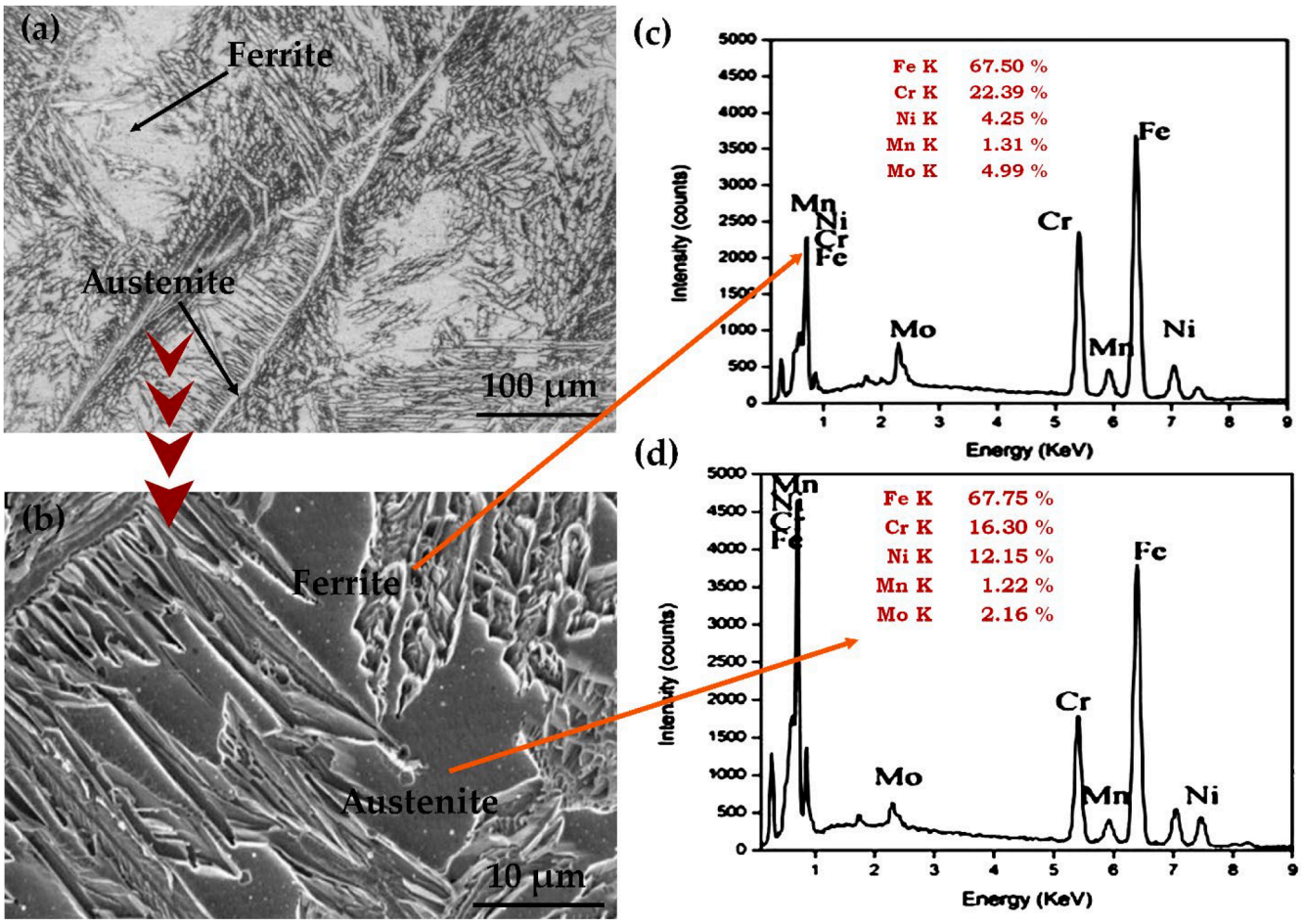

Fig. 8. SEM and EDS Analysis of E2209 Weld.

indicate the two-phase nature of the E2209 filler [46]. During welding, bonding produces a balanced phase structure while tertiary matrix elements Cr and Mo enable ferrite generation, with Ni maintaining the stability of austenite formation. At increased magnification (10 μm), as seen in Fig. 8(b), the morphology of the ferrite and austenite is more clearly observable. Ferrite manifests as linked networks, while austenite develops elongated or plate-like structures. The meticulous distribution of phases improves the thermal stability of the weld, offering resistance to cracking and pitting corrosion, which are crucial for preserving the integrity of the welded joint under demanding working circumstances. The EDS spectra in Fig. 8(c) and 8(d) validate the elemental composition of the ferrite and austenite phases, respectively. The ferrite phase, seen in Fig. 8(c), exhibits an elevated Cr concentration of 22.39 wt. % and a Fe content of 67.50 wt. %, with minor contributions from Mo at 4.99 wt. % and Ni at 4.25 wt. %. Cr and Mo improve the corrosion resistance of the ferrite phase, especially in chloride-laden conditions. The austenite phase, seen in Fig. 8(d), has a greater Ni concentration (12.15 wt. %) than ferrite, with substantial quantities of Cr (16.30 wt. %) and Fe (67.75 wt. %). Ni is an austenite stabilizer, promoting ductility and toughness in the weld region. Analysis through SEM and EDS showcases that the E2209 WZ features a potent balanced dual-phase microstructure. The ferrite phase enhances the WZ with strength and corrosion protection against pits, but the austenite phase adds ductility alongside toughness to the weld. The E2209 weld's synergistic microstructure allows it to perform during demanding operating conditions, making it the best choice for dissimilar weld applications between SS316L and SS439.

3.5. Grain structure analysis of E309L weld

The grain structure of the E309L WZ is examined using Electron Backscatter Diffraction (EBSD), which produced maps that show grain orientation together with phase and grain size distributions. According to these studies, the microstructural features of the weld region as well as the interface and HAZ show links to the mechanical performance of welded construction joints [47,48]. The E309L WZ and adjacent areas, including the interface and HAZ, display their grain orientations in Fig. 9 (a). The microstructure of the WZ shows mostly fine grains with elongated shapes that demonstrate significant angular misorientation because of the targeted way that the material solidifies during welding. Recrystallization and thermal effects lead larger grain sizes to manifest in the immediate HAZ. In the WZ, 79 % of grain boundaries show high angles, while 21 % display low angles. HAGBs dominate the weld structure, raising mechanical strength by making fracture developments less probable at these grain boundaries. The phase map represented in Fig. 9(b) shows how austenite (γ) and ferrite (δ) phases spread across the WZ. The material structure displays ferrite at 57 % composition next to 41 % austenite. The balance between phases in the weld defines the duplex stainless-steel nature of the E309L filler material. The ferrite phase delivers enhanced resistance against cracking and corrosion, but the austenite phase contributes to better ductility and toughness. Welds achieve mechanical soundness and corrosion protection through the stable arrangement of their phases. The distribution of grain sizes within the fusion spot and surrounding HAZ appears in Fig. 9(c). Massive illustrative grain measurements from the weld region measure approximately 286 ± 223 μm at the weld core and display coarse grain features on adjoining interface boundaries. The difference in WZ and HAZ grain

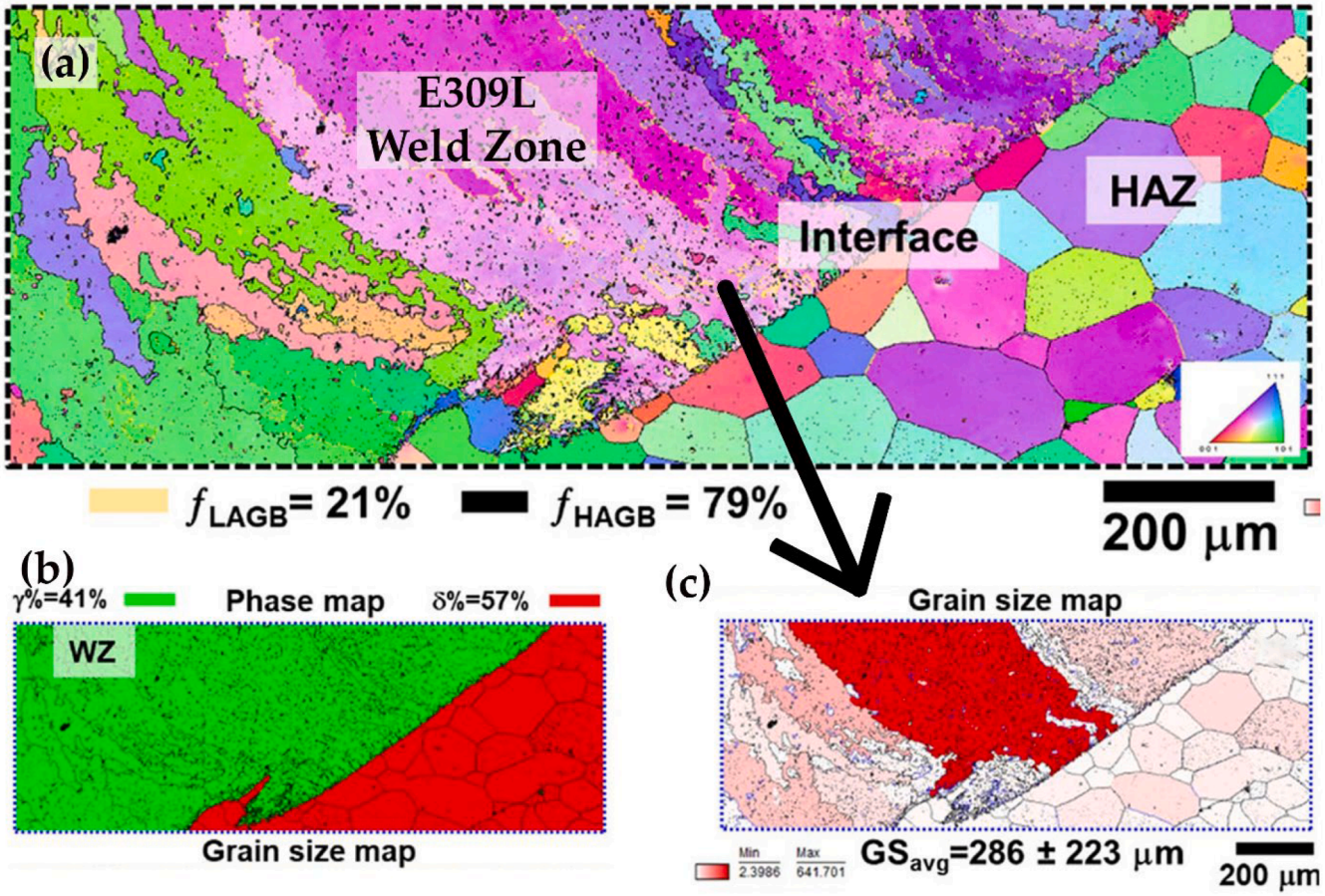

Fig. 9. Grain structure analysis of E309L weld.

size results from both temperature gradients and cooling rates during welding. Mechanical integrity increases due to small grains in the WZ, while heat-safe properties grow due to coarse grains in the HAZ. Grain structure analysis reveals that the E309L WZ displays a unique microstructure that shows high fractions of high-angle grain boundaries, balanced austenite and ferrite phases, and varied grain dimensions. By improving mechanical attributes and performance against different forces, the weld becomes outstanding for dissimilar welding applications.

3.6. Grain structure analysis of E2209 weld

The representation in Fig. 10(a) shows how grains are oriented in the E2209 WZ and the interface and adjacent HAZ region. A refined grain structure predominates in the WZ, which includes 72 % of high-angle grain boundaries, while low-angle grain boundaries comprise only 27 %. HAGBs enhance mechanical strength and resistance to fracture propagation. The interface and HAZ exhibit coarser grains relative to the WZ, with grain growth seen in the HAZ due to the thermal cycle encountered during welding. The refined grains in the WZ boost their mechanical performance and toughness.

Fig. 10(b) depicts the phase distribution throughout the WZ and HAZ. The E2209 filler has a duplex structure, with the austenite (γ) phase comprising 40 % of the microstructure and the ferrite (δ) phase accounting for 57 %. The austenite phase is present primarily in the WZ, while the ferrite phase is dispersed across the WZ and HAZ. This phase distribution guarantees a equilibrium of strength, thermal stability, and corrosion resilience which are typical of duplex stainless-steel weldments [49]. Fig. 10(c) illustrates the dispersal of grain sizes throughout the WZ and HAZ. The mean size of grain in the WZ is 177 ± 148 μm, with finer grains primarily located in the weld core and coarser grains present around the interface and HAZ. The reduced grain size in the WZ is a consequence of regulated cooling during the welding process, which improves strength and toughness. The larger grains in the HAZ result from grain growth and recrystallization encouraged by the thermal effects of welding. The differences in grain size indicate the temperature gradients and solidification rates during welding. The grain structure analysis of the E2209 weld reveals a refined and balanced microstructure with a high fraction of HAGBs, a well-distributed duplex phase (austenite and ferrite), and a fine-grained WZ. These features contribute to the weld's excellent mechanical properties, including strength, toughness, and resistance to cracking and corrosion, making the E2209 filler a practical choice for welding dissimilar materials like SS316L and SS439.

3.7. Mechanical test results of E309L and E2209 welds

The mechanical property tests, including UTS, impact strength, and EL %, followed standard testing procedures. Three specimens were prepared and tested for each test to ensure result reliability. The reported values in the manuscript represent the average of three measurements, with standard deviations included to indicate data consistency (Fig. 11). The E2209 weld exhibited superior UTS (582 MPa) compared to the E309L weld (525 MPa), attributed to its duplex stainless-steel structure with a balanced austenite-ferrite microstructure. The presence of delta ferrite in E2209 improved tensile strength by restricting grain boundary movement [50]. Conversely, the E309L weld, with its predominantly austenitic matrix, displayed lower tensile strength due to limited ferrite content. Regarding impact strength, the E2209 weld (74 J) outperformed the E309L weld (62 J) due to its duplex

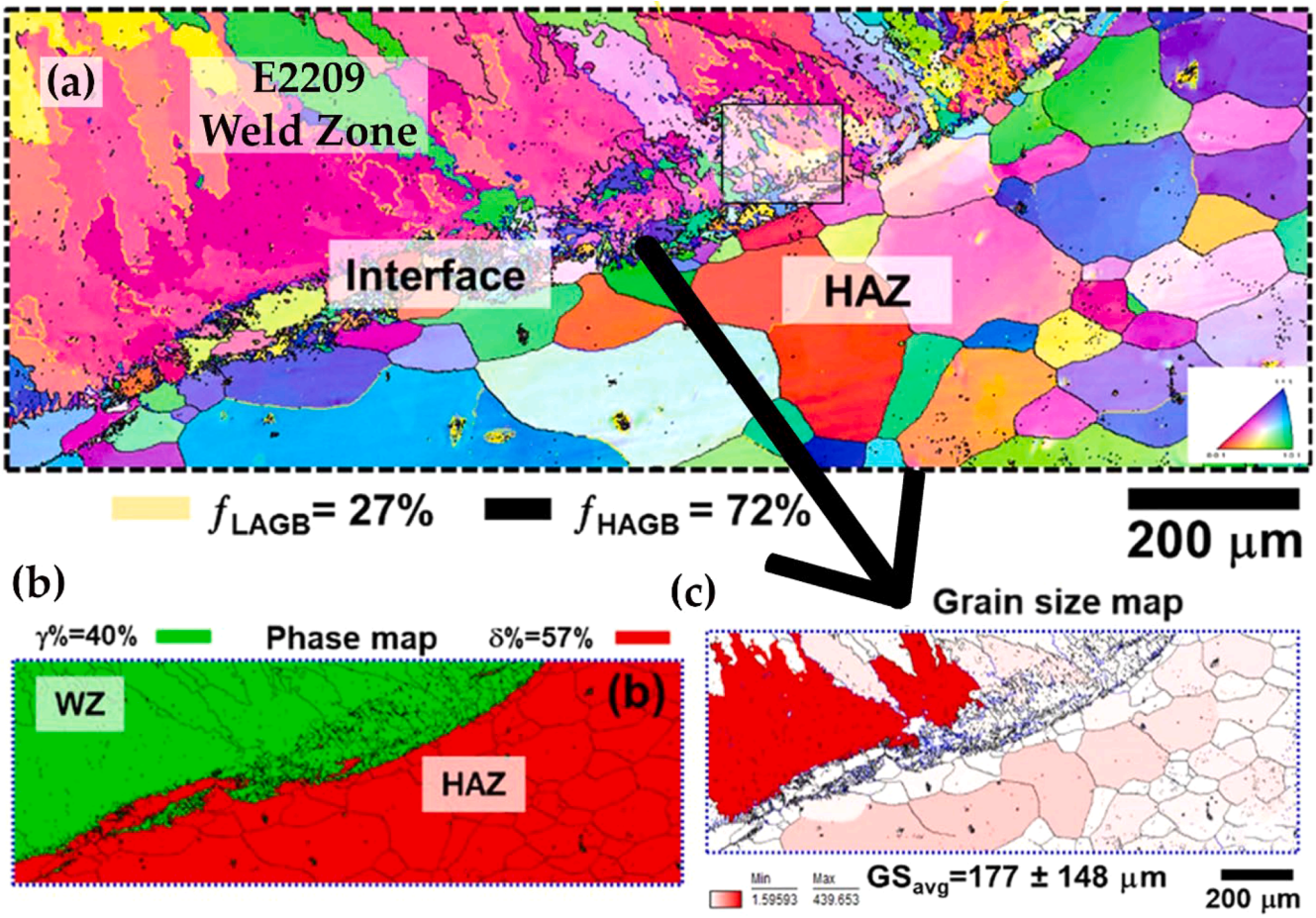

Fig. 10. Grain structure analysis of E2209 weld.

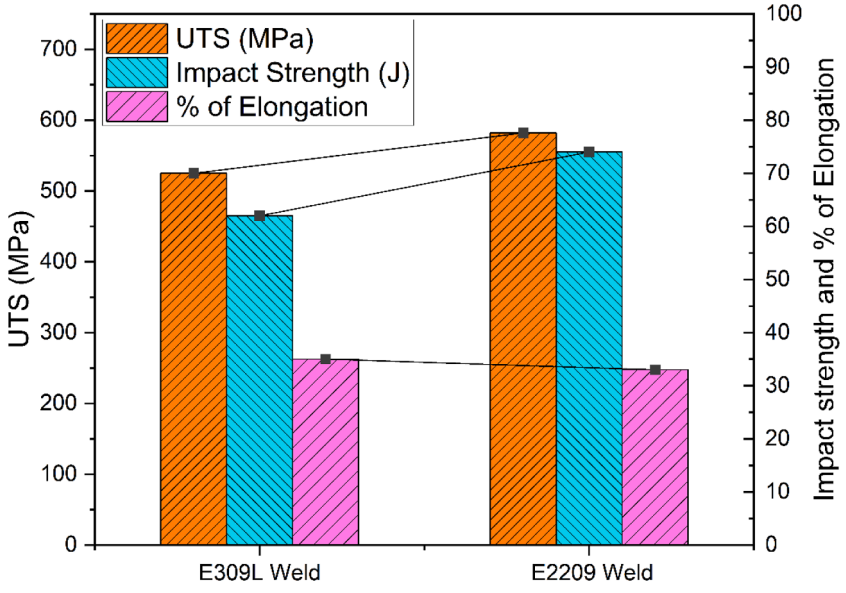

Fig. 11. Mechanical test result.

microstructure combining fracture-resistant ferrite with ductile austenite. The enhanced chromium and molybdenum content in E2209 further improved resistance to brittle fracture, ensuring better toughness under dynamic loading conditions. The E309L weld's lower impact strength is linked to its austenitic structure, which is less effective in resisting sudden impacts. The fracture occurred in the SS439 BM, attributed to its higher hardness and reduced ductility compared to SS316L. Although the HAZ is typically prone to failure, improved phase stability in the WZs and minimized thermal defects due to the CMT process enhanced the integrity of these regions. The hardness

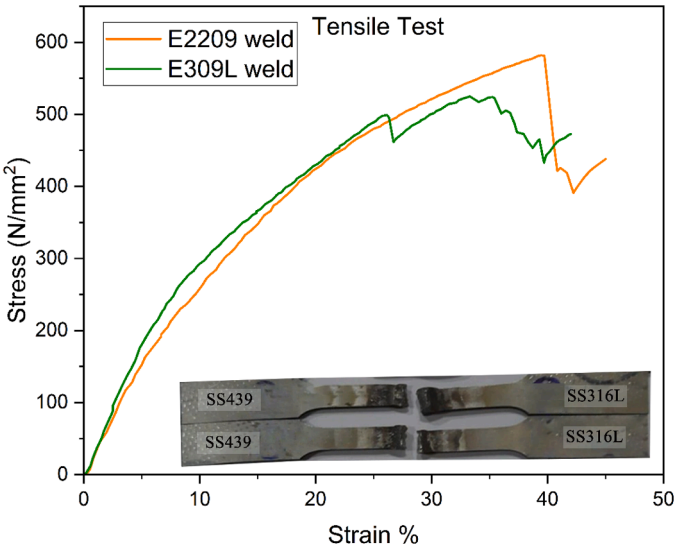

Fig. 12. Stress strain curve for tensile test.

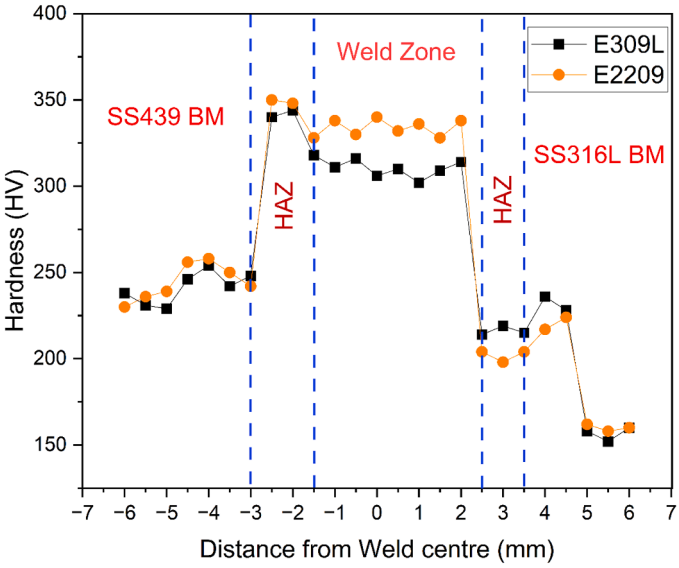

Fig. 14. Microhardness of dissimilar joints.

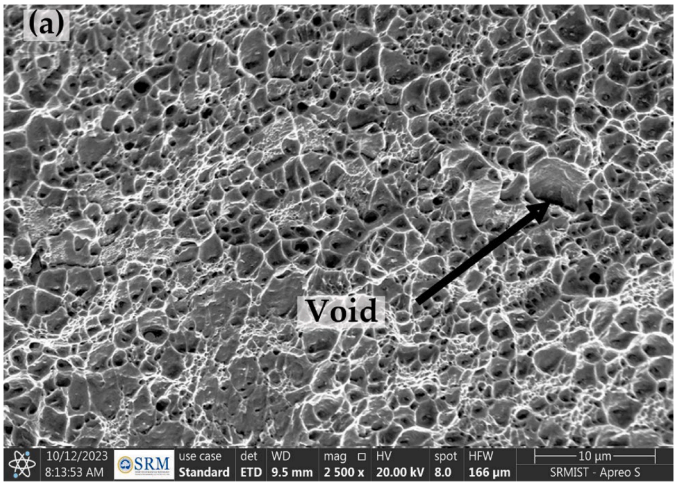

Fig. 13. Tensile test fractured SEM image (a) E309L weld (b) E2209 weld.

distribution trends confirmed that the SS439 BM was the most vulnerable under tensile stress conditions.

The EL % of the E309L weld (35 %) is marginally higher than E2209 weld (33 %). The increased elongation in the E309L weld arises from its fully austenitic structure, which offers superior ductility and enables more significant deformation before fracture [51]. In contrast, the duplex structure of the E2209 weld, while providing exceptional strength and hardness, slightly compromises ductility due to the presence of ferrite, which exhibits lower elongation characteristics compared to austenite. These findings highlight that the E2209 weld demonstrates superior tensile strength and impact energy, making it desirable for applications necessitating enhanced mechanical strength and toughness [52]. Conversely, the E309L weld offers slightly better ductility, which may be advantageous in scenarios where more excellent elongation under stress is critical. Findings highlights the need of tailoring filler material selection to application-specific mechanical specifications.

This stress-strain plot (Fig. 12) compares tensile features across multiple welding points produced with E2209 and E309L filler materials. The weld executed with E2209 contains superior ultimate tensile strength because it demonstrates a sharper stress increase, reaching approximately 582 MPa, thus indicating improved load-bearing performance owing to its duplex structural qualities. The E309L weld achieves an ultimate tensile strength of 525 MPa because its fully austenitic microstructure shows reduced overall strength. The E309L weld demonstrates exceptional elongation at fracture, which signals improved ductility, making it suitable for increased deformation capabilities until failure. The fragmented specimens demonstrate complete splits within the insert illustration, which authenticates the tensile test validity and assesses the welds' comparative ductility and strength properties.

3.7.1. Tensile test fracture SEM analysis

SEM analysis of fracture specimen surfaces reveals how the failure mechanisms occurred in both E309L and E2209 welded joints. The E309L weld fracture surface shown in Fig. 13(a) displays ductile failure characteristics because of void coalescence alongside dimple formation. Observations of multiple voids combined with interconnected dimple formations indicate ductile failure occurred through micro-void nucleation followed by expansion and coalescence. The E309L weld shape demonstrates its complete austenitic structure through enhanced ductility, which permits plastic deformation before its breaking point. Fig. 13(b) demonstrates E2209 weld characteristics that show more precise dimple formation with fewer voids, leading to superior strength yet some reduction in ductility compared to the E309L weld. Due to its duplex microstructure, which includes ferrite and austenite phases, the

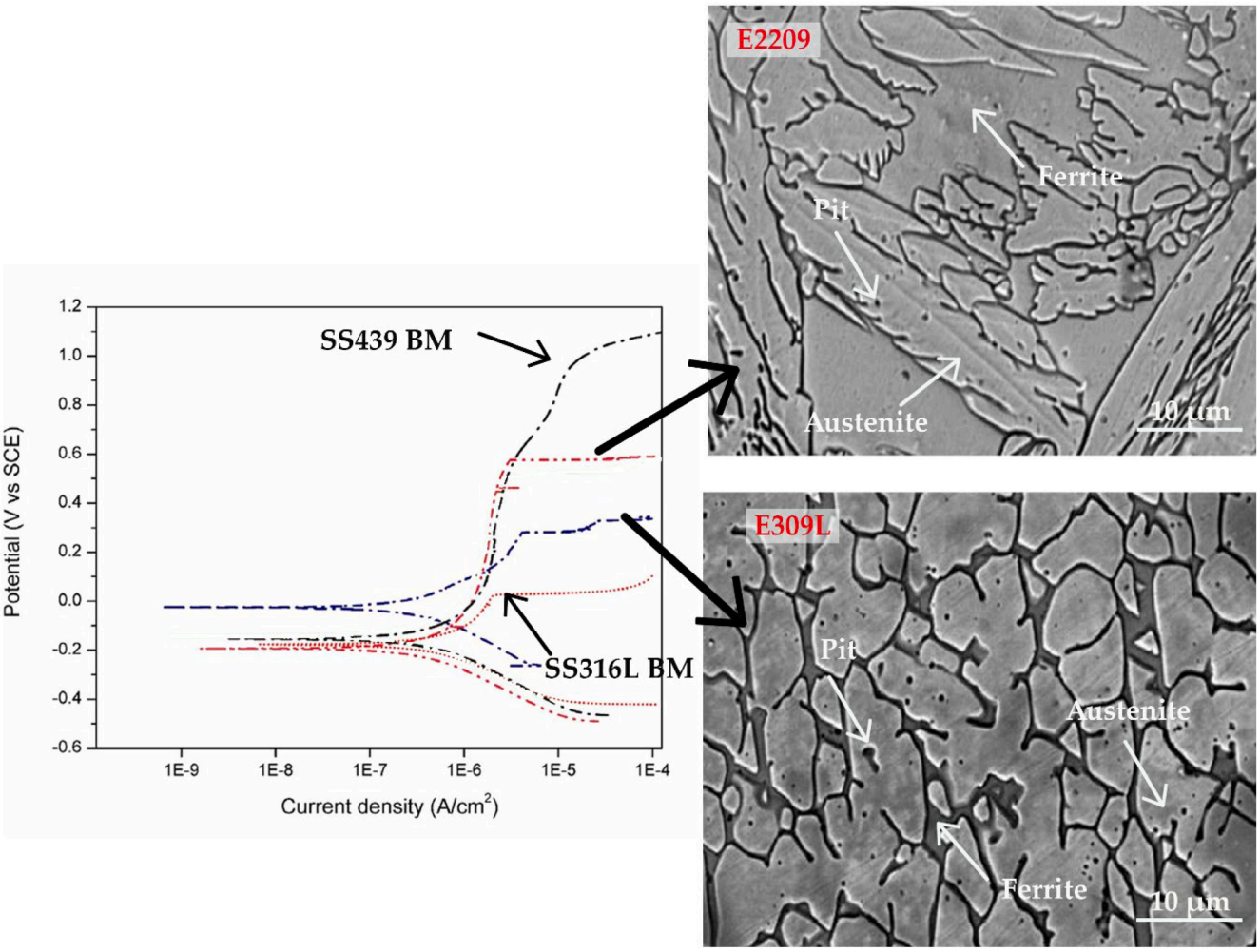

Fig. 15. The Potentiodynamic polarization curves and SEM images of different weld.

E2209 weld increases strength without sacrificing necessary toughness. The smaller and deeper dimples observed suggest a higher resistance to crack initiation and propagation, resulting in a more controlled fracture mechanism under tensile stress [53,54]. Overall, the SEM analysis confirms the superior ductility of the E309L weld and the enhanced strength-toughness balance of the E2209 weld, aligning with their respective microstructural characteristics and mechanical test results.

3.7.2. *Microhardness analysis*

The microhardness distribution across the WZ, HAZ, and BMs is shown in Fig. 14. The hardness in the WZ for both fillers is significantly substantial than in BMs and HAZ, with the E2209 weld exhibiting slightly higher hardness values (approximately 350 HV) than the E309L weld (~330 HV), attributed to their duplex microstructure, containing a balanced distribution of ferrite and austenite phases, enhancing its strength and deformation resistance.

In the HAZ regions adjacent to SS316L and SS439, a noticeable drop in hardness is observed for both fillers due to thermal softening and grain coarsening induced by the welding heat cycle. The hardness of the SS439 BM (~250 HV) is higher than SS316L (~200 HV), reflecting their inherent material properties, with SS439's ferritic structure being more rigid but less ductile as that of austenitic structure of SS316L [54]. The gradual hardness change over the weld interface and into the BMs ensures a smooth transition of mechanical properties, reducing the risk of failure under operational stresses. This hardness profile highlights the superior performance of E2209 in applications where enhanced strength and resistance towards wear is needed in the WZ.

3.8. *Corrosion behaviour*

Potentiodynamic polarization tests were conducted to evaluate the corrosion characteristics of dissimilar E309L and E2209 welds in a 3.5 wt. % NaCl solution, simulating seawater conditions. The corrosion behaviour was analyzed by examining anodic polarization curves and identifying the respective pitting potentials (Epit) [55,56]. The results indicated that the SS439 BM revealed superior resistance to pitting and passivity than SS316L BM. This improved resistance is attributed to its balanced phase structure and higher nitrogen content, which enhance pitting resistance through an increased Pitting Resistance Equivalent Number (PREN). The PREN, calculated based on N, Mo, and Cr content, effectively predicts chloride-induced pitting resistance. Among the weldments, the E2209 weld demonstrated significantly better pitting resistance (Epit = 559 mV) than the E309L weld (Epit = 265 mV), primarily due to its duplex microstructure [57,58]. The stable ferrite-austenite phase structure in the E2209 weld enhances Mo and Cr content, strengthening passive film formation and improving resistance to chloride-induced pitting [59].

In contrast, the fully E309L weld austenitic structure rendered it more susceptible to pitting corrosion. The polarization curves (Fig. 15) further established the larger corrosion resistance of the E2209 weld, which exhibited a sophisticated corrosion potential (Ecorr = −250.145 mV) and a inferior corrosion current density (Icorr = 0.752 μA) associated to the E309L weld (Ecorr = −267.326 mV, Icorr = 1.25 μA), signifying a reduced corrosion rate. SEM analysis revealed fewer and smaller corrosion pits in the E2209 weld, predominantly in the ferrite

regions, due to its enriched contents of Mo and Cr enhancing passivation. Conversely, the E309L weld exhibited more frequent and larger pits distributed in both austenitic and ferritic regions, confirming its lower pitting resistance. These results indicate that the E2209 filler offers superior corrosion resistance in chloride environments, making it the ideal choice for applications exposed to aggressive seawater conditions. While the E309L filler demonstrates commendable corrosion resistance, its higher susceptibility to localized pitting underscores the advantage of E2209 in environments demanding enhanced corrosion performance. These findings provide critical insights for selecting appropriate filler materials in corrosion-prone environments [60].

4. Conclusion

This study comprehensively evaluated the mechanical, microstructural, and corrosion characteristics of SS316L and SS439 weldments produced using the CMT welding process with E309L and E2209 filler materials. The results reveal a strong correlation between microstructural features and the resulting mechanical and corrosion performance. The E309L weld exhibited a fully austenitic microstructure, which contributed to improved ductility (35 % elongation) but resulted in lower tensile strength (525 MPa) and reduced corrosion resistance. The absence of ferrite in the E309L weld led to a softer WZ with uniform but lower hardness values. The reduced chromium and molybdenum content further increased its susceptibility to pitting corrosion. In contrast, the E2209 weld displayed a duplex microstructure comprising balanced ferrite and austenite phases. This microstructure improved grain stability and enhanced mechanical performance, achieving a superior UTS (582 MPa) and impact energy (74 J). The presence of ferrite increased hardness and improved resistance to grain boundary movement, resulting in better mechanical stability. The more Mo and Cr content in the E2209 weld enhanced passivation behaviour, contributing to its improved pitting resistance and lower corrosion rate.

These findings highlight that the E2209 filler is optimal for applications necessitating superior strength, toughness, and corrosion resilience, particularly in marine, chemical, and power generation environments. Conversely, the E309L filler is better suited for higher ductility applications with moderate corrosion resistance. This study emphasizes aligning filler material selection with specific application requirements to ensure optimal weld performance. Future research may explore the long-term performance of these weldments under cyclic stress, elevated temperatures, and more aggressive corrosion environments. Additionally, investigating alternative filler materials and novel welding techniques may further augment the stainless-steel joints performance.

Human and animal ethics statement

During this investigation, no experiments were conducted with human or animal subjects.

CRediT authorship contribution statement

Saravanakumar Sengottaiyan: Supervision, Methodology, Conceptualization. **V.S. Shaisundaram:** Writing – original draft, Formal analysis, Data curation. **M. Shameer Basha:** Visualization, Validation, Investigation. **B. Deepanraj:** Writing – review & editing, Supervision, Project administration. **N. Senthilkumar:** Writing – original draft, Methodology, Investigation.

Declaration of competing interest

The research authors have made no statements about conflicts of interest throughout this publication.

Data availability

The data related to this study is available within this article.

References

[1] X. Wen, S. Liu, X. Gao, B. Zhang, Y. Wang, Y. Chen, S. Qiao, F. Wang, N. Li, Y. Shi, C. Yuan, Investigation of microstructure and mechanical properties in dissimilar-metal welding between ferritic stainless steel and Co-based superalloy using electron beam welding, J. Mater. Res. Technol. 26 (2023) 5177–5192, https://doi.org/10.1016/j.jmrt.2023.08.254.

[2] A. Rajesh Kannan, N. Siva Shanmugam, S. Naveenkumar, Effect of arc length correction on weld bead geometry and mechanical properties of AISI 316L weldments by cold metal transfer (CMT) process, Mater. Today Proc. 18 (2019) 3916–3921, https://doi.org/10.1016/j.matpr.2019.07.331.

[3] I.J. Singh, Q. Murtaza, P. kumar, A comprehensive review on effect of cold metal transfer welding parameters on dissimilar and similar metal welding, J. Eng. Res. (Ponta Grossa) (2023), https://doi.org/10.1016/j.jer.2023.12.009.

[4] Y. Zhao, H. Sun, X. Zhou, H. Zhao, F. Liu, B. Yang, B. Chen, C. Tan, The effect of inhomogeneous microstructure on the properties of laser-MIG hybrid welded 316L/AH36 dissimilar joints, J. Mater. Res. Technol. 28 (2024) 4088–4096, https://doi.org/10.1016/j.jmrt.2023.12.235.

[5] V. Krishnan, E. Ayyasamy, V. Paramasivam, Influence of resistance spot welding process parameters on dissimilar austenitic and duplex stainless steel welded joints, Proc. Inst. Mech. Eng., Part E: J. Process Mech. Eng. 235 (2021) 12–23, https://doi.org/10.1177/0954408920933528.

[6] K. Karthick, S. Malarvizhi, V. Balasubramanian, S.A. Krishnan, G. Sasikala, S. K. Albert, Tensile properties of shielded metal arc welded dissimilar joints of nuclear grade ferritic steel and austenitic stainless steel, J. Mech. Behav. Mater. 25 (2016) 171–178, https://doi.org/10.1515/jmbm-2017-0005.

[7] H. Shanker, R. Wattal, A comprehensive survey on the cold metal transfer process in welding similar and dissimilar materials and for cladding, Proc. Inst. Mech. Eng. C. J. Mech. Eng. Sci. 237 (2023) 2360–2391, https://doi.org/10.1177/09544062221139947.

[8] H. Li, X.S. Liu, Y.S. Zhang, M.T. Ma, G.Y. Li, J. Senkara, Current research and challenges in innovative technology of joining dissimilar materials for electric vehicles, in: advanced high strength steel and press hardening, World Sci. (2019) 363–380, https://doi.org/10.1142/9789813277984_0056.

[9] T.V.B. Babu, N. Gobu, S. Kaliappan, L. Natrayan, Mechanical fatigue and microstructure behaviour of Cassava peel SiO_2 strengthened friction stir welded AA 6065-Al_2O_3 metal matrix composite joints, Surface Rev. Lett. (2025), https://doi.org/10.1142/S0218625X25501537.

[10] M.E. Kocadağistan, O. Çinar, T. Teker, Weldability and mechanical behavior of CMT welded AISI 430 and HARDOX 500 steels, Mater. Test. 65 (2023) 1302–1310, https://doi.org/10.1515/mt-2023-0169.

[11] N. Senthilkumar, K. Sabari, P. Azhagiri, M. Yuvaperiyasamy, Impact of tool geometry and friction stir welding parameters on AZ31 magnesium alloy weldment wear behaviour and process optimization, Welding Int. 38 (2024) 805–822, https://doi.org/10.1080/09507116.2024.2430208.

[12] M. Lervåg, C. Sørensen, A. Robertstad, B.M. Brønstad, B. Nyhus, M. Eriksson, R. Aune, X. Ren, O.M. Akselsen, I. Bunaziv, Additive manufacturing with superduplex stainless steel wire by CMT process, Metals. (Basel) 10 (2020) 272, https://doi.org/10.3390/met10020272.

[13] S.T. Selvamani, M. Bakkiyaraj, G. Yoganandan, D.R. N, an empirical study of CMT-welded interface features and corrosion characteristics of dissimilar joints, Proc. Inst. Mech. Eng., Part E: J. Process Mech. Eng. 239 (2025) 118–128, https://doi.org/10.1177/09544089231170986.

[14] N. Xu, J. Shen, J. Zhou, S. Hu, Microstructure and pitting corrosion resistance of AISI 430 ferritic stainless steel joints fabricated by ultrasonic vibration assisted cold metal transfer technique, Metals. (Basel) 12 (2022) 382, https://doi.org/10.3390/met12030382.

[15] W. Xu, H. He, Y. Yi, H. Wang, C. Yu, W. Fang, Dissimilar joining of stainless steel and aluminum using twin-wire CMT, Welding World 65 (2021) 1541–1551, https://doi.org/10.1007/s40194-021-01089-0.

[16] G.L. Liu, S.W. Yang, W.T. Han, L.J. Zhou, M.Q. Zhang, J.W. Ding, Y. Dong, F. R. Wan, C.J. Shang, R.D.K. Misra, Microstructural evolution of dissimilar welded joints between reduced-activation ferritic-martensitic steel and 316L stainless steel during the post weld heat treatment, Mater. Sci. Eng.: A 722 (2018) 182–196, https://doi.org/10.1016/j.msea.2018.03.035.

[17] S.L. Hernández-Trujillo, V.H. Lopez-Morelos, M.A. García-Rentería, R. García-Hernández, A. Ruiz, F.F. Curiel-López, Microstructure and fatigue behavior of 2205/316L stainless steel dissimilar welded joints, Metals. (Basel) 11 (2021) 93, https://doi.org/10.3390/met11010093.

[18] M. Sun, S. Liu, Y. Cheng, Z. Cheng, R. Ren, C. Chen, Microstructure characteristics and mechanical properties of the thin-plate AISI 430 ferritic stainless steel joints by interrupted pulsed arc welding, J. Mater. Res. Technol. 21 (2022) 4500–4511, https://doi.org/10.1016/j.jmrt.2022.11.063.

[19] H. Xiang, C. Xu, T. Zhan, L. Wu, H. Wang, L. Li, Influence of metal transfer modes on pore formation during the welding process of AA6082/A360 dissimilar aluminum alloys, J. Mater. Eng. Perform. 32 (2023) 8750–8766, https://doi.org/10.1007/s11665-022-07757-6.

[20] C. Ye, W. Zhai, G. Lu, Q. Liu, L. Ni, L. Ye, X. Fang, Microstructural evolution and mechanical integrity relationship of dissimilar metal welding between 2205 duplex

stainless steel and composite bimetallic plates, Proc. Inst. Mech. Eng. C. J. Mech. Eng. Sci. 235 (2021) 7033–7044, https://doi.org/10.1177/09544062211003615.
[21] J. Verma, R.V. Taiwade, Effect of austenitic and austeno-ferritic electrodes on 2205 duplex and 316L austenitic stainless steel dissimilar welds, J. Mater. Eng. Perform. 25 (2016) 4706–4717, https://doi.org/10.1007/s11665-016-2329-4.
[22] M. Shojaati, B. Beidokhti, Characterization of AISI 304/AISI 409 stainless steel joints using different filler materials, Constr. Build. Mater. 147 (2017) 608–615, https://doi.org/10.1016/j.conbuildmat.2017.04.185.
[23] C. Tembhurkar, R. Kataria, S. Ambade, J. Verma, A. Sharma, S. Sarkar, Effect of fillers and autogenous welding on dissimilar welded 316L austenitic and 430 ferritic stainless steels, J. Mater. Eng. Perform. 30 (2021) 1444–1453, https://doi.org/10.1007/s11665-020-05395-4.
[24] C. Wang, Y. Yu, J. Yu, Y. Zhang, Y. Zhao, Q. Yuan, Microstructure evolution and corrosion behavior of dissimilar 304/430 stainless steel welded joints, J. Manuf. Process. 50 (2020) 183–191, https://doi.org/10.1016/j.jmapro.2019.12.015.
[25] S.K. Gupta, A.P. Patil, R.C. Rathod, A. Gupta, H. Methani, V. Tandon, Cold metal transfer welding of ferritic and austenitic stainless steel: microstructural, mechanical, and electrochemical studies, J. Mater. Eng. Perform. 33 (2024) 10663–10679, https://doi.org/10.1007/s11665-024-09743-6.
[26] S. Ambade, C. Tembhurkar, A. Rokde, S. Gupta, S. Shelare, C. Prakash, L.R. Gupta, V.A. Smirnov, Experimental investigation of microstructural, mechanical and corrosion properties of 316L and 202 austenitic stainless steel joints using cold metal transfer welding, J. Mater. Res. Technol. 27 (2023) 5881–5888, https://doi.org/10.1016/j.jmrt.2023.11.091.
[27] J. Verma, R.V. Taiwade, R.K. Khatirkar, A. Kumar, A comparative study on the effect of electrode on microstructure and mechanical properties of dissimilar welds of 2205 austeno-ferritic and 316L austenitic stainless steel, Mater. Trans. 57 (2016) 494–500, https://doi.org/10.2320/matertrans.M2015321.
[28] S. Aguilar, R. Tabares, C. Serna, Microstructural transformations of dissimilar austenite-ferrite stainless steels welded joints, J. Mater. Phys. Chem. 1 (2013) 65–68, https://doi.org/10.12691/jmpc-1-4-2.
[29] Y. Koli, N. Yuvaraj, S. Aravindan, Vipin, CMT joining of AA6061-T6 and AA6082-T6 and examining mechanical properties and microstructural characterization, Trans. Indian Inst. Metals 74 (2021) 313–329, https://doi.org/10.1007/s12666-020-02134-0.
[30] Y. Koli, N. Yuvaraj, S. Aravindan, Vipin, multi-response mathematical model for optimization of process parameters in CMT welding of dissimilar thickness AA6061-T6 and AA6082-T6 alloys using RSM-GRA coupled with PCA, Adv. Indust. Manuf. Eng. 2 (2021) 100050, https://doi.org/10.1016/j.aime.2021.100050.
[31] V.V. Satyanarayana, G.Madhusudhan Reddy, T. Mohandas, Dissimilar metal friction welding of austenitic–ferritic stainless steels, J. Mater. Process. Technol. 160 (2005) 128–137, https://doi.org/10.1016/j.jmatprotec.2004.05.017.
[32] M. Ramamurthy, P. Balasubramanian, N. Senthilkumar, G. Anbuchezhiyan, Influence of process parameters on the microstructure and mechanical properties of friction stir welds of AA2014 and AA6063 aluminium alloys using response surface methodology, Mater. Res. Express. 9 (2022) 026528, https://doi.org/10.1088/2053-1591/ac5777.
[33] K. Aliakbari, S. Kamel Abbasnia, M. Shariati, Evaluation of the ratcheting behavior of Cr-Mo steel used in CNG tank, Results. Eng. 25 (2025) 104218, https://doi.org/10.1016/j.rineng.2025.104218.
[34] K. Sabari, A. Muniappan, B. Deepanraj, M. Yuvaperiyasamy, Exploring the effect of TiO_2 nanoparticles on the microstructural dynamics and mechanical attributes of dissimilar FSW joints between AA7071 and AZ31, Trans. Indian Inst. Metals 78 (2025) 66, https://doi.org/10.1007/s12666-024-03535-1.
[35] G. Natarajan, G. Krishnan, K. Seeniappan, N. Lakshmaiya, Influence of heat treated manihot esculenta Biosilica on friction stir welded AA 6065-Al2O3 metal matrix composite and microstructural, mechanical, and fatigue analysis, Mater. Res. 28 (2025), https://doi.org/10.1590/1980-5373-mr-2024-0473.
[36] H. Hamedi, T. Isfahani, Wear and corrosion properties of mechanically coated 316 stainless Steel-TiC nanocomposites, Results. Eng. 24 (2024) 102966, https://doi.org/10.1016/j.rineng.2024.102966.
[37] J.L. Jeronimo, A.P. Krelling, C. Pacheco, I. Bonetti, R. da Silva, J.C.G. Milan, C. E. da Costa, Microstrutural, mechanical characterizations and corrosion behaviour of borides layers on Inconel 718 superalloy, Results. Eng. 16 (2022) 100783, https://doi.org/10.1016/j.rineng.2022.100783.
[38] J. Verma, R.V. Taiwade, R.K. Khatirkar, S.G. Sapate, A.D. Gaikwad, Microstructure, mechanical and intergranular corrosion behavior of dissimilar DSS 2205 and ASS 316L shielded metal arc welds, Trans. Indian Inst. Metals 70 (2017) 225–237, https://doi.org/10.1007/s12666-016-0878-8.
[39] N. Ghosh, P. Kumar Pal, G. Nandi, R. Rudrapati, Parametric optimization of gas metal arc welding process by PCA based Taguchi method on Austenitic Stainless Steel AISI 316L, Mater. Today Proc. 5 (2018) 1620–1625, https://doi.org/10.1016/j.matpr.2017.11.255.
[40] M. Sireesha, V. Shankar, S.K. Albert, S. Sundaresan, Microstructural features of dissimilar welds between 316LN austenitic stainless steel and alloy 800, Mater. Sci. Eng.: A 292 (2000) 74–82, https://doi.org/10.1016/S0921-5093(00)00969-2.
[41] A.V. Bansod, A.P. Patil, Effect of welding processes on microstructure, mechanical properties, and corrosion behavior of low-nickel austenitic stainless steels, Metallogr., Microstruct., Anal. 6 (2017) 304–314, https://doi.org/10.1007/s13632-017-0368-3.
[42] N. Kumar, A. Kumar, A. Gupta, A.D. Gaikwad, R.K. Khatirkar, Gas tungsten arc welding of 316L austenitic stainless steel with UNS S32205 duplex stainless steel, Trans. Indian Inst. Metals 71 (2018) 361–372, https://doi.org/10.1007/s12666-017-1167-x.
[43] E.M.F. de Souza Silva, G.S. da Fonseca, E.A. Ferreira, Microstructural and selective dissolution analysis of 316L austenitic stainless steel, J. Mater. Res. Technol. 15 (2021) 4317–4329, https://doi.org/10.1016/j.jmrt.2021.10.009.
[44] M. Sarkari Khorrami, M.A. Mostafaei, H. Pouraliakbar, A.H. Kokabi, Study on microstructure and mechanical characteristics of low-carbon steel and ferritic stainless steel joints, Mater. Sci. Eng.: A 608 (2014) 35–45, https://doi.org/10.1016/j.msea.2014.04.065.
[45] M. Prabhakaran, J. Duraisamy, N.S. Shanmugam, A.R. Kannan, M. Varatharajalu, Weld strength and microstructure analysis on resistance spot welding of austenitic AISI 347 stainless steel and Duplex AISI 2205 stainless steel, Trans. Indian Inst. Metals 76 (2023) 925–936, https://doi.org/10.1007/s12666-022-02789-x.
[46] C. Wichan, S. Loeshpahn, Effect of filler alloy on microstructure, mechanical and corrosion behaviour of dissimilar weldment between Aisi 201 stainless steel and low carbon steel sheets produced by a gas tungsten arc welding, Adv. Mat. Res. 581–582 (2012) 808–816, https://doi.org/10.4028/www.scientific.net/AMR.581-582.808.
[47] H. Khosrovaninezhad, M. Shamanian, A. Rezaeian, J. Kangazian, M. Nezakat, J. A. Szpunar, Insight into the effect of weld pitch on the microstructure-properties relationships of St 37/AISI 316 steels dissimilar welds processed by friction stir welding, Mater. Charact. 177 (2021) 111188, https://doi.org/10.1016/j.matchar.2021.111188.
[48] J. Kangazian, M. Shamanian, Electron back scattered diffraction study of dissimilar welding between the Super duplex stainless steel and the Ni-based superalloy, Met. Mater. Int. 25 (2019) 1287–1300, https://doi.org/10.1007/s12540-019-00289-0.
[49] J. Verma, R.V. Taiwade, R. Kataria, A. Kumar, Welding and electrochemical behavior of ferritic AISI 430 and austeno-ferritic UNS 32205 dissimilar welds, J. Manuf. Process. 34 (2018) 292–302, https://doi.org/10.1016/j.jmapro.2018.06.019.
[50] P. Kumar, B. Kumar, S. Pratap, S.M.M. Hasnain, B.A. Alkhaleel, Synthesis and predictive modelling of wear behaviour in hybrid aluminum composites, Results. Eng. (2025) 104612, https://doi.org/10.1016/j.rineng.2025.104612.
[51] S. Kaliappan, T. Mothilal, L. Natrayan, P. Pravin, T.T. Olkeba, Mechanical characterization of friction-stir-welded aluminum AA7010 alloy with TiC nanofiber, Adv. Mater. Sci. Eng. 2023 (2023) 1–7, https://doi.org/10.1155/2023/1466963.
[52] A. Moteshakker, I. Danaee, S. Moeinifar, A. Ashrafi, Hardness and tensile properties of dissimilar welds joints between SAF 2205 and AISI 316L, Sci. Technol. Welding Joining 21 (2016) 1–10, https://doi.org/10.1179/1362171815Y.0000000062.
[53] V. Tandon, M.A. Thombre, A.P. Patil, R.V. Taiwade, H. Vashishtha, Effect of heat input on the microstructural, mechanical, and corrosion properties of dissimilar weldment of conventional austenitic stainless steel and low-nickel stainless steel, Metallogr., Microstruct., Anal. 9 (2020) 668–677, https://doi.org/10.1007/s13632-020-00681-y.
[54] J.G. Roy, N. Yuvaraj, Vipin, effect of welding parameters on mechanical properties of cold metal transfer welded thin AISI 304 stainless-steel sheets, Trans. Indian Inst. Metals 74 (2021) 2397–2408, https://doi.org/10.1007/s12666-021-02326-2.
[55] N. Ebrahimi, M.H. Moayed, A. Davoodi, Critical pitting temperature dependence of 2205 duplex stainless steel on dichromate ion concentration in chloride medium, Corros. Sci. 53 (2011) 1278–1287, https://doi.org/10.1016/j.corsci.2010.12.019.
[56] J.H. Potgieter, P.A. Olubambi, L. Cornish, C.N. Machio, E.-S.M. Sherif, Influence of nickel additions on the corrosion behaviour of low nitrogen 22 % Cr series duplex stainless steels, Corros. Sci. 50 (2008) 2572–2579, https://doi.org/10.1016/j.corsci.2008.05.023.
[57] R. Kaçar, Effect of solidification mode and morphology of microstructure on the hydrogen content of duplex stainless steel weld metal, Mater. Des. 25 (2004) 1–9, https://doi.org/10.1016/S0261-3069(03)00169-9.
[58] P.B. Srinivasan, V. Muthupandi, W. Dietzel, V. Sivan, An assessment of impact strength and corrosion behaviour of shielded metal arc welded dissimilar weldments between UNS 31803 and IS 2062 steels, Mater. Des. 27 (2006) 182–191, https://doi.org/10.1016/j.matdes.2004.10.019.
[59] H. Yang, F. Shu, J. Deng, X. Zhang, Y. Ren, B. Lei, X. Yuan, Improving the corrosion resistance and mechanical properties of 2205 duplex stainless steel welded joints by laser cladding CoCrFeNiTiSi high-entropy alloys coating, Surf. Coat. Technol. (2025) 132137, https://doi.org/10.1016/j.surfcoat.2025.132137.
[60] S.A. Erfani Mobarakeh, K. Dehghani, Microstructural evolutions and corrosion behavior of nanocomposite AlCoCrFeNi2.1 high-entropy alloy produced via friction stir processing, J. Mater. Res. Technol. 30 (2024) 8345–8358, https://doi.org/10.1016/j.jmrt.2024.05.170.